Reconstructing coherent dynamics of bound states induced by strong attosecond XUV pulses

Lijuan Jia (贾利娟)[1], Mingqing Liu (刘明清)[1], Xinqiang Wang (王新强)[1], Long Xu (徐 龙)[2], Peiguang Yan (闫培光)[1], Wei-Chao Jiang (姜维超)[1*], and Libin Fu (傅立斌)[3**]

[1] Institute of Quantum Precision Measurement, College of Physics and Optoelectronic Engineering, Shenzhen University, Shenzhen 518060, China

[2] Department of Physics, Xiamen University, Xiamen 361005, China

[3] Graduate School of China Academy of Engineering Physics, Beijing 100193, China

*Corresponding author: jiang.wei.chao@szu.edu.cn

**Corresponding author: lbfu@gscaep.ac.cn

We propose a scheme that utilizes weak-field-induced quantum beats to investigate the electronic coherences of atoms driven by a strong attosecond extreme ultraviolet (XUV) pulse. The technique involves using a strong XUV pump pulse to excite and ionize atoms and a time-delayed weak short pulse to probe the photoelectron signal. Our theoretical analysis demonstrates that the information regarding the bound states, initiated by the strong pump pulse, can be precisely reconstructed from the weak-field-induced quantum beat spectrum. To examine this scheme, we apply it to the attosecond XUV laser-induced ionization of hydrogen atoms by solving a three-dimensional time-dependent Schrödinger equation. This work provides an essential reference for reconstructing the ultrafast dynamics of bound states induced by strong XUV attosecond pulses.

1. Introduction

Probing and controlling electron behavior in matter at attosecond timescales has become possible with attosecond pulses generated by few-cycle intense lasers. This breakthrough has revolutionized our understanding of the atomic structure and molecular processes[1–10]. Various experiments have been carried out, claiming exceptional time resolution down to a few tens of attoseconds, using tools such as attosecond photoelectron streaking[11,12], the reconstruction of attosecond beating by interference of two-photon transitions (RABBIT)[13,14], high-harmonic spectroscopy[15], attoclocks[16,17], and attosecond transient absorption spectroscopy (ATAS)[18,19]. When observing ultrafast electronic motion, understanding the dynamics of excited states is a fundamental issue in various laser–matter interaction processes[20–28]. Specifically, the emission time of high-harmonic radiation from excited states is temporally delayed, providing a means to monitor excited-state dynamics[26,29,30]. The role of laser-dressed excited energy levels in atomic excitation and ionization has been studied using attosecond technology[4,31,32]. In the process of strong-field tunneling ionization, the transition of electrons to the continuum via multiple bound states has been investigated[33–36].

With the advancement of pump-probe experiments and the development of attosecond pulses, it has become possible to detect information about the bound states of atoms. De Boer and Muller[37] obtained the populations of excited states by calculating the area probability of each peak in the photoelectron energy distribution using a nanosecond probe pulse. This method requires long lifetimes of the bound states. More recently, under the high sensitivity of attosecond transient absorption spectroscopy (ATAS), the real-time population of valence states has been experimentally measured using a combination of a few-cycle near-infrared (NIR) pulse and a single XUV attosecond pulse[38].

Quantum-beat spectroscopy in a pump-probe setting is an alternative interferometric tool for obtaining bound-state dynamics. Building upon earlier research that employed high-harmonic radiation[39], XUV frequency combs[40], and synchrotron radiation[41], the coherence and amplitudes of bound states have been extracted from the emission attosecond quantum beat spectrum in hydrogen[42], where two optical attosecond pulses are used. Quantum-beat signals carrying bound state information have also been mapped onto the photoelectron spectrum[43–46]. A wave packet in low-lying excited states of the

helium atom, oscillating with an ultrashort period of 2.0 fs, has been mapped out[43]. Zhang *et al.*[45] have reconstructed time-evolved density matrix elements in one-dimensional (1D) atomic hydrogen by exploiting femtosecond XUV pulses and a terahertz (THz) streaking field. Recently, the populations of bound states caused by an XUV pump pulse have been retrieved with high precision from the photoelectron quantum beat spectrum in the 1D hydrogen atom[46]. In our previous work, the NIR probe pulse used was strong and long to ensure the complete ionization of electrons. However, achieving complete ionization in the experiment is challenging, making it more of a qualitative model in principle.

In this work, we propose a different setting, using strong attosecond XUV pump and weak attosecond XUV probe pulses to reconstruct the populations of bound states from the quantum-beat signals in the photoelectron spectrum. In this approach, the probe pulse is weak and short, which differs from the treatment of the strong-field approximation[47–49] in Ref. [45]. We examine this scheme for strong attosecond XUV laser-induced ionization of hydrogen atoms by solving a three-dimensional time-dependent Schrödinger equation (TDSE). We demonstrate that the dynamics of bound states can be reconstructed with high precision. This general approach provides a valuable reference for reconstructing the ultrafast dynamics of bound states induced by strong XUV attosecond pulses.

2. Formulation

2.1. Quantum beats in the photoelectron spectrum

In our scheme, we employ a strong attosecond few-cycle XUV pulse, referred to as the pump pulse in Fig. 1(a), to coherently excite and ionize the atom, as shown in Fig. 1(b). This attosecond pump pulse facilitates a dominant one-photon absorption process. A weaker attosecond XUV pulse with a time delay τ_d relative to the pump pulse serves as the probe pulse. The probe pulse couples the induced excited states, such as $|b\rangle$ and $|j\rangle$, with the continuum state $|\mathbf{q}\rangle$, leading to the transfer of coherent population to the same ionized state $|\mathbf{p}\rangle$. Consequently, the state $|\mathbf{p}\rangle$ is populated through multiple ionization pathways, as shown in Fig. 1(b). The ionization process carries valuable information about the coherent states. After the complete pump-probe pulse sequence, the photoelectron signal exhibits oscillations, commonly called "quantum beats," as a function of the time delay τ_d between the pump and probe pulses. These quantum beats provide insights into the dynamics of the coherent wave packet and the energy spacing involved. By analyzing these quantum beats, we can extract information about the temporal evolution of the electron wave packet and the associated energy dynamics. In the following, we will illustrate this coherent process through the temporal evolution of the electron wave packet.

The electron wave packet for the atom initially in its ground state $|1\rangle$ induced by the pump pulse can be written as
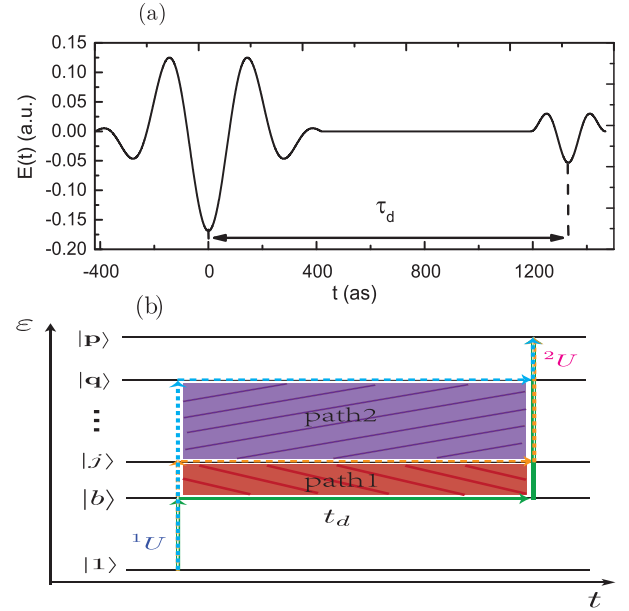

Fig. 1. (a) Temporal profile of attosecond XUV pulse in the *z*-direction. τ_d is the time interval between the two pulses. (b) Sketch of interference pathways. Impulsive excitation (^1U) forms a coherent superposition of bound states ($|1\rangle$, $|b\rangle$, $|j\rangle$, ...) and continuum ($|\mathbf{q}\rangle$). A second attosecond XUV pulse (^2U) transfers the coherent population to the continuum $|\mathbf{p}\rangle$. The dynamical quantum beat is determined by the shaded areas in the energy–time diagram enclosed by different pathways. The quantum beat phase of path 1 is the red shaded area, $|\varepsilon_j - \varepsilon_b|t_d$, and the phase of path 2 is the purple shaded area, $|\frac{q^2}{2} - \varepsilon_j|t_d$.

$$|\psi_1\rangle = \sum_j \langle j|^1U|1\rangle|j\rangle + \int d\mathbf{p}\langle \mathbf{p}|^1U|1\rangle|\mathbf{p}\rangle$$
$$\equiv \sum_j {}^1U_{j1}|j\rangle + \int d\mathbf{p}\, {}^1U_{\mathbf{p}1}|\mathbf{p}\rangle, \tag{1}$$

where $|j\rangle$ denotes the *j*th bound state with energy ε_j. The state $|\mathbf{p}\rangle$ represents the continuum state with momentum p. ^1U stands for the evolution operator in the presence of the pump pulse. Next, the electrons evolve freely over a duration, t_d [$t_d = \tau_d - (T_1 + T_2)/2$], which induces a stationary evolution phase to the state. This can be expressed as

$$|\psi_1(t_d)\rangle = \sum_j {}^1U_{j1}e^{-i\varepsilon_j t_d}|j\rangle + \int d\mathbf{p}\, {}^1U_{\mathbf{p}1}e^{-i\frac{p^2}{2}t_d}|\mathbf{p}\rangle, \tag{2}$$

where τ_d is sufficiently long to ensure that the second pulse does not overlap with the first one, as shown in Fig. 1(a). After the second weak and ultrashort probe pulse, the wave packet of electrons becomes

$$|\psi_2(t_d)\rangle = \sum_b \left(\sum_j {}^j\Lambda_{b1}e^{-i\varepsilon_j t_d} + \int d\mathbf{p}\, {}^{\mathbf{p}}\Lambda_{b1}e^{-i\frac{p^2}{2}t_d} \right)|b\rangle$$
$$+ \int d\mathbf{p} \left(\sum_j {}^j\Lambda_{\mathbf{p}1}e^{-i\varepsilon_j t_d} + \int d\mathbf{q}\, {}^{\mathbf{q}}\Lambda_{\mathbf{p}1}e^{-i\frac{q^2}{2}t_d} \right)|\mathbf{p}\rangle, \quad (3)$$

where ${}^{\gamma}\Lambda_{\alpha\beta} \equiv {}^2U_{\alpha\gamma}{}^1U_{\gamma\beta}$, ${}^2U_{bj} = \langle b|^2U|j\rangle$, ${}^2U_{b\mathbf{p}} = \langle b|^2U|\mathbf{p}\rangle$, and $|b\rangle$ represents the bth bare bound state. ${}^2U_{\mathbf{p}j} = \langle \mathbf{p}|^2U|j\rangle$, ${}^2U_{\mathbf{p}\mathbf{q}} = \langle \mathbf{p}|^2U|\mathbf{q}\rangle$, and $|\mathbf{q}\rangle$ represents the continuum state with momentum q. ${}^2U$ represents the evolution operator perturbed by the second pulse. For numerical calculations, we can project Eq. (3) onto the scattering state of the atom to detect the photo-electron yield, which is given by

$$P(\mathbf{p},t_d) = \sum_b \sum_j {}^b\Lambda_{\mathbf{p}1}{}^j\Lambda^*_{\mathbf{p}1}e^{-i(\varepsilon_b-\varepsilon_j)t_d} + \left| \int d\mathbf{q}\, {}^{\mathbf{q}}\Lambda_{\mathbf{p}1}e^{-i\frac{q^2}{2}t_d} \right|^2$$
$$+ \sum_j \left[\int d\mathbf{q}\, {}^j\Lambda_{\mathbf{p}1}{}^{\mathbf{q}}\Lambda^*_{\mathbf{p}1}e^{-i(\varepsilon_j-\frac{q^2}{2})t_d} + \text{c.c.} \right]. \quad (4)$$

The time-resolved photoelectron signal exhibits quantum beats due to interfering pathways. Fourier analysis of the quantum beat signal $P(\mathbf{p},t_d)$ can analyze the quantum beat pattern. However, in the realistic numerical calculations, the range of the time delay τ_d is finite [compared to the analytical derivation where the range is $(-\infty,\infty)$], which introduces abrupt changes in the photoelectron signals. To suppress this background noise, we apply a Gaussian envelope given by $g(\tau_d) = \exp\left[-2\ln 2\frac{(\tau_d - t')^2}{\tau_F^2}\right]$, where τ_F represents the full-width at half-maximum of the laser pulse. Here, $t' = t_0 + T/2$, with t_0 and T denoting the starting point and duration of the time delay, respectively. The resulting quantum beat spectrum is given by

$$G(\mathbf{p},\Omega) = \mathcal{F}[P(\mathbf{p},t_d) \cdot g(\tau_d)],$$
$$= \mathcal{F}[P(\mathbf{p},t_d)]^*\mathcal{F}[g(\tau_d)] \equiv \widetilde{G}(\mathbf{p},\Omega)^*\widetilde{g}(\Omega), \quad (5)$$

where

$$\widetilde{G}(\mathbf{p},\Omega) = \sum_b \sum_j {}^b\Lambda_{\mathbf{p}1}{}^j\Lambda^*_{\mathbf{p}1}\delta[\Omega - (\varepsilon_j - \varepsilon_b)]$$
$$+ \iint d\mathbf{q}d\mathbf{q}'\, {}^{\mathbf{q}}\Lambda_{\mathbf{p}1}{}^{\mathbf{q}'}\Lambda^*_{\mathbf{p}1}\delta\left[\Omega - \left(\frac{q'^2}{2} - \frac{q^2}{2}\right)\right]$$
$$+ \sum_j \left\{ \int d\mathbf{q}\, {}^j\Lambda_{\mathbf{p}1}{}^{\mathbf{q}}\Lambda^*_{\mathbf{p}1}\delta\left[\Omega - \left(\frac{q^2}{2} - \varepsilon_j\right)\right] \right.$$
$$\left. + \int d\mathbf{q}\, {}^{\mathbf{q}}\Lambda_{\mathbf{p}1}{}^j\Lambda^*_{\mathbf{p}1}\delta\left[\Omega - \left(-\frac{q^2}{2} + \varepsilon_j\right)\right] \right\}, \quad (6)$$

and

$$\widetilde{g}(\Omega) = \frac{1}{2\sqrt{\pi a}}e^{-i\Omega t' - \frac{\Omega^2}{4a}}, \quad a = \frac{2\ln 2}{\tau_F^2}. \quad (7)$$

We can observe that the information regarding the energy gap is encoded in the quantum beat spectrum. After performing the convolution, as shown in Eq. (5), we obtain

$$G(\mathbf{p},\Omega)$$
$$= \frac{1}{2\sqrt{\pi a}} \times \left\{ \sum_b \sum_j e^{-i[\Omega - (\varepsilon_j - \varepsilon_b)]t'}e^{-\frac{[\Omega - (\varepsilon_j - \varepsilon_b)]^2}{4a}}\,{}^b\Lambda_{\mathbf{p}g}{}^j\Lambda^*_{\mathbf{p}g} \right.$$
$$+ \iint d\mathbf{q}d\mathbf{q}'e^{-i\left[\Omega - \left(\frac{q'^2}{2} - \frac{q^2}{2}\right)\right]t'}e^{-\frac{\left[\Omega - \left(\frac{q'^2}{2} - \frac{q^2}{2}\right)\right]^2}{4a}}\,{}^{\mathbf{q}}\Lambda_{\mathbf{p}g}{}^{\mathbf{q}'}\Lambda^*_{\mathbf{p}g}$$
$$+ \sum_j \int d\mathbf{q}e^{-i\left[\Omega - \left(\frac{q^2}{2} - \varepsilon_j\right)\right]t'}e^{-\frac{\left[\Omega - \left(\frac{q^2}{2} - \varepsilon_j\right)\right]^2}{4a}}\,{}^j\Lambda_{\mathbf{p}g}{}^{\mathbf{q}}\Lambda^*_{\mathbf{p}g}$$
$$\left. + \sum_j \int d\mathbf{q}e^{-i\left[\Omega - \left(-\frac{q^2}{2} + \varepsilon_j\right)\right]t'}e^{-\frac{\left[\Omega - \left(-\frac{q^2}{2} + \varepsilon_j\right)\right]^2}{4a}}\,{}^{\mathbf{q}}\Lambda_{\mathbf{p}g}{}^j\Lambda^*_{\mathbf{p}g} \right\}. \quad (8)$$

The Gaussian envelope is used solely for noise reduction, which does not alter the underlying physical results. As a result, we can extract the interference information exclusively from $\widetilde{G}(\mathbf{p},\Omega)$ as given by Eq. (6).

2.2. Retrieving the bound-state population

Quantum beats provide valuable information about impulsively induced coherence. In the next step, we aim to reconstruct the populations of bound states induced by the pump pulse by isolating the different interference processes present in the quantum beat spectrum. The population of the bth bound state, denoted as $|{}^1U_{b1}|^2$, is related to the quantity ${}^b\Lambda_{\mathbf{p}1}$, which is defined as ${}^b\Lambda_{\mathbf{p}1} \equiv {}^2U_{\mathbf{p}b}{}^1U_{b1}$. As a result, the population of the bound state $|b\rangle$ can be expressed as

$$|{}^1U_{b1}|^2 = \frac{|{}^b\Lambda_{\mathbf{p}1}|^2}{|{}^2U_{\mathbf{p}b}|^2}. \quad (9)$$

In our previous scheme[46], the probe pulse was designed to be extremely long so that electrons are completely ionized at the end of the pulse, i.e., $\int |{}^2U_{\mathbf{p}b}|^2 d\mathbf{p} \approx 1$. In this case, once ${}^b\Lambda_{\mathbf{p}1}$ is known, the population of the bound state $|b\rangle$ is given by

$$|{}^1U_{b1}|^2 = \int |{}^b\Lambda_{\mathbf{p}1}|^2 d\mathbf{p}. \quad (10)$$

By referring to Eq. (6), $|{}^b\Lambda_{\mathbf{p}1}|$ can be obtained from the first term in the quantum beat spectrum. However, obtaining the quantum beat spectrum in full-dimensional space is challenging in practical experiments. It requires detecting the three-dimensional photoelectron momentum distribution. Second, for every polarized angle θ, every azimuthal angle φ, and every momentum p, one needs to collect signals at different time delays and

then perform a Fourier transform of the time delay to obtain the 3D quantum beat spectrum. The system exhibits cylindrical symmetry for a linearly polarized laser pulse, and a single arbitrary azimuthal angle φ is sufficient. Furthermore, it should be noted that the electrons need to be completely ionized.

We now propose an improvement to the previous reconstruction scheme to make it more feasible experimentally. In our scheme, we only detect the photoelectron momentum distribution along the polarization direction of the laser field, i.e., the z-axis. Instead of using an extremely long and strong probe pulse, we suggest using a weak and ultrashort attosecond pulse for the probing measurement, which only perturbs the system. In this case, the population of the bound state $|b\rangle$ is given by

$$|^1U_{b1}|^2 = \frac{|^b\Lambda_{\mathbf{p}1}|^2}{|^2U_{\mathbf{p}b}|^2}. \tag{11}$$

First, we calculate $|^b\Lambda_{\mathbf{p}1}|$ from the quantum beat spectrum. According to Eq. (6), the first term only contains information about the bound states characterized by a delta function. The finite range of τ_d in numerical calculations results in a non-negligible spacing $d\Omega$. As a result, the characteristic signals appearing in the quantum beat spectrum will span a certain width along Ω. To obtain $^b\Lambda_{\mathbf{p}1}$, we integrate the beat frequency Ω near $\delta\varepsilon_{bj}$ on both sides of Eq. (8), where $\delta\varepsilon_{bj} = \varepsilon_b - \varepsilon_j$, and $b \neq j$ (with $b,j = 1,2,3,\dots$). This integration leads to the following expression,

$$\int_{\delta\varepsilon_{bj}-d\varepsilon}^{\delta\varepsilon_{bj}+d\varepsilon} G(\mathbf{p},\Omega)d\Omega$$
$$\approx \frac{1}{2\sqrt{\pi a}}\int_{\delta\varepsilon_{bj}-d\varepsilon}^{\delta\varepsilon_{bj}+d\varepsilon} e^{-i(\Omega-\delta\varepsilon_{bj})t'} e^{-\frac{(\Omega-\delta\varepsilon_{bj})^2}{4a}} {}^b\Lambda_{\mathbf{p}1}{}^j\Lambda_{\mathbf{p}1}^* d\Omega. \tag{12}$$

After further calculations, we obtain

$$\left| \int_{\delta\varepsilon_{bj}-d\varepsilon}^{\delta\varepsilon_{bj}+d\varepsilon} G(\mathbf{p},\Omega)d\Omega \right| = |^b\Lambda_{\mathbf{p}1}||^j\Lambda_{\mathbf{p}1}|, \tag{13}$$

where $2\delta\varepsilon$ represents the approximate distribution width, which observes that the artificial envelope $g(\tau_d)$ no longer appears in Eq. (13), confirming that the envelope does not impact the physical results. For each pair of distinct bound states, one equation involving $^b\Lambda_{\mathbf{p}1}$ can be obtained. When $C_n^2 \geq n$ (where n is the number of bound states), specifically for $n \geq 3$, it is possible to solve for $^b\Lambda_{\mathbf{p}1}$.

Second, we calculate the photoionization cross section $|^2U_{\mathbf{p}b}|$. An analytical expression for the photoionization cross section of the ground state can be found in Refs. [50,51]. Experimental detection of the photoionization cross sections for excited states can be found in Ref. [52]. In our numerical simulations, we calculate $|^2U_{\mathbf{p}b}|$ using the time-dependent perturbation theory. In the weak and short probing measurement regime, the one-photon transition is the dominant process. The transition amplitude in the velocity gauge can be expressed as[53,54]

$$^2U_{\mathbf{p}b} = -\int_{-T_2/2}^{T_2/2} \langle p|\mathbf{A}(t) \cdot \nabla|b\rangle e^{i(E-\varepsilon_b)t}dt, \tag{14}$$

where $E = p^2/2$. This equation indicates that we can reconstruct the population of the bound state induced by the pump pulse by calculating Eq. (11).

3. Examining the Reconstruction Scheme in Atomic Hydrogen

3.1. Quantum beat spectrum for atomic hydrogen

We now examine this reconstruction scheme for realistic atomic hydrogen by solving the time-dependent Schrödinger equation (TDSE) in the velocity gauge and dipole approximation,

$$i\partial_t\psi(\mathbf{r},t) = [H_0 - i\mathbf{A}(t) \cdot \nabla]\psi(\mathbf{r},t), \tag{15}$$

where $H_0 = -\nabla^2/2 - 1/\mathbf{r}$ is the field-free Hamiltonian. The vector potential is given by $\mathbf{A}(t) = A(t)\hat{z}$, with

$$A(t,\tau_d) = A_1 f_1(t) \sin(\omega_1 t) + A_2 f_2(t - \tau_d) \sin[\omega_2(t - \tau_d)], \tag{16}$$

where a sin-squared envelope is used,

$$f_i(t) = \sin^2\left(\frac{\pi t}{T_i}\right), \tag{17}$$

with T_i being the duration of the ith laser pulse. $A_i = \sqrt{I_i}/\omega_i$ represents the vector potential amplitude, where I_i is the peak intensity, and ω_i is the photon energy for the ith pulse. The time interval τ_d corresponds to the interval between the envelope maxima of the first and second pulses, as depicted in Fig. 1(a).

To propagate the wave function in time, we employ the split-Lanczos propagator[55–57]. In our calculations, the wave function is expressed as a unique sum of spherical harmonics, and the radial part of the wave function is discretized using the finite-element discrete variable representation (FE-DVR) method[58–60]. To solve the TDSE, we split the solution into inner and outer regions at specific time points t_i (with $i = 1,2,\dots,N_{\text{split}}$) using an absorbing function $s(r)$,

$$\psi(\mathbf{r},t) = s(r)\psi(\mathbf{r},t) + [1 - s(r)]\psi(\mathbf{r},t). \tag{18}$$

The absorbing function $s(r)$ is defined as follows:

$$s(r) = 1 - \frac{1}{1 + e^{(r-R_c)/\Delta}}, \tag{19}$$

where R_c represents the size of the inner box. The inner wave function follows the TDSE strictly, while the outer part is propagated using the Coulomb–Volkov propagator[61,62].

Our numerical simulations set the maximal angular momentum as $l_{\max} = 10$. The radial box size is $r_{\max} = 350$ atomic units (a.u.), and the inner box size is $R_c = 200$ a.u. The time step used

in the simulations is $\Delta t = 0.01$ a.u. The pump pulse used in our simulations has an intensity of 10^{15} W/cm^2 and a wavelength of 100 nm. The pulse duration, denoted as T_1, is set to 2.5 optical cycles, which is approximately equal to 834.4 as. The pump pulse prepares a superposition of bound states and continuum. The photon energy of the first pulse, ω_1, is blue detuned with respect to the $|3p\rangle$ state and red detuned with respect to the $|4p\rangle$ state. Under these parameters, the primary contribution to electron dynamics arises from the one-photon transition. After interacting with the pump pulse, electrons predominantly populate the bound states $|1s\rangle$, $|2p\rangle$, $|3p\rangle$, and $|4p\rangle$, as illustrated in Fig. 2. The probe pulse, on the other hand, is extremely short, lasting only one optical cycle (approximately 275.7 as). Like the pump pulse, the probe process is primarily governed by a one-photon transition.

After the interaction is completed, we obtain the final momentum distribution $P(p, \tau_d)$ along the polarized direction of the laser field for different time delays τ_d, as shown in Fig. 3(a). The photoelectron signals exhibit quantum beats and demonstrate the presence of attosecond coherence in both bound states and continuum. Interestingly, they display a distribution of light–dark cycles as a function of τ_d. In our calculations, we consider a range of time delays from $\tau_d(\text{start}) = 58$ a.u. to $\tau_d(\text{end}) = 3598$ a.u., with a spacing of 4 a.u., resulting in a total of 886 interval points. This number is significantly
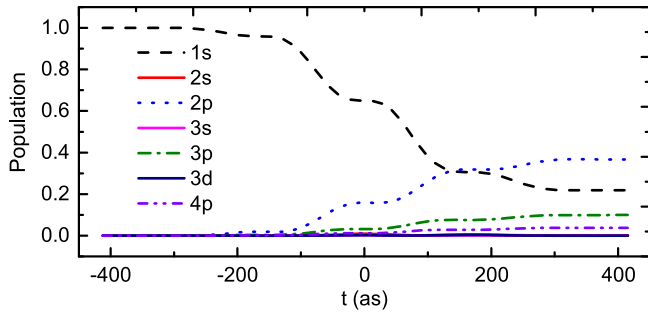
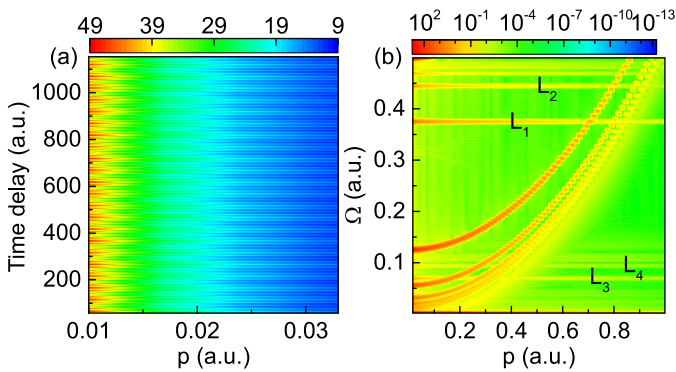**Fig. 2.** Populations of bound states driven by the pump pulse.

Fig. 3. (a) Photoelectron's momentum distribution in the laser field's polarized direction with different time delay. (b) Frequency-resolved photon-electronic spectroscopy $G(\mathbf{p}, \Omega)$. The laser parameters of the first pulse are $\lambda_1 = 100$ nm and $T_1 = 2.5$ optical cycles.

smaller than the 2048 time delay samples used in our previous scheme. The choice of a large time delay ($\tau_d \geq 58$ a.u.) ensures that the coherent state prepared by the first pulse remains unaffected by the probe pulse, indicating no overlap between the two laser pulse sequences. To extract the interference information encoded in the momentum distribution[Fig. 3(a)], we perform a Fourier transform of the quantum beat signal $P(\mathbf{p}, \tau_d)$, yielding a momentum-frequency correlation spectrum $G(\mathbf{p}, \Omega)$. To mitigate the effect of the sudden change in the photoelectron signals induced by the time delay, we apply a Gaussian window function $g(\tau_d)$ with a width equal to one-fourth of the range $[\tau_d(\text{end}) - \tau_d(\text{start})]$. The resulting quantum beat pattern is given by $G(\mathbf{p}, \Omega) = (2\pi)^{-1} \int P(\mathbf{p}, \tau_d) g(\tau_d) \exp(-i\Omega\tau_d) \mathrm{d}\tau_d$.

Figure 3(b) shows the frequency-resolved photon-electronic spectroscopy, i.e., the quantum-beat spectrum $G(\mathbf{p}, \Omega)$. By applying the Gaussian window, we effectively reduce the background noise compared to Fig. 1(c) in Ref. [46]. The spectrum exhibits two prominent interference structures, for which horizontal lines, labeled as $L_1, L_2, \ldots$, are observed at a constant frequency Ω, and upward-opening parabolic curves are also observed. These characteristics observed in the full-dimensional system are consistent with those obtained in the 1D case[46]. Notably, the characteristic signals in the spectrum have a certain width, which is wider than the 1D case, despite the use of the same spacing $d\Omega = 0.00178$ a.u.

As can be seen from Eq. (6), we can identify the physical origins of the two prominent interference structures observed in Fig. 3(b). The horizontal lines in the spectrum correspond to the first term of Eq. (6), specifically when $\Omega = \varepsilon_j - \varepsilon_b$ in the δ function. This can be visualized as interference path 1, as depicted in Fig. 1(b). Initially, electrons populated in the ground state $|1\rangle$ transition to different excited states $|b\rangle$ and $|j\rangle$ under the influence of the first laser pulse ^1U. During the subsequent free evolution time t_d, a dynamical quantum beat phase is accumulated, which is equal to the red shaded area in Fig. 1(b) and given by $|\varepsilon_j - \varepsilon_b|t_d$. With the second pulse ^2U, the excited electrons from states $|j\rangle$ and $|b\rangle$ are ultimately ionized into the same continuum state $|\mathbf{p}\rangle$, resulting in interference. This accumulated phase manifests as the horizontal lines in the quantum beat spectrum, indicating interference between electron wave packets originating from two different bound states.

Similarly, the parabolic curves in the spectrum result from the third term of Eq. (6), occurring when $\Omega = \frac{q^2}{2} - \varepsilon_j$. This corresponds to interference path 2 in Fig. 1(b). Electrons are ionized into the continuum state $|\mathbf{q}\rangle$ and excited to the state $|j\rangle$ by the first pulse ^1U. During the subsequent free evolution, these electrons accumulate a relative phase given by the purple shaded area in Fig. 1(b) and equal to $|\frac{q^2}{2} - \varepsilon_j|t_d$. After the second pulse ^2U, which transitions the electrons from $|\mathbf{q}\rangle$ and $|j\rangle$ to the same $|\mathbf{p}\rangle$ continuum state, interference occurs. This interference between electron wave packets originating from the continuum and the bound state gives rise to the observed parabolic curves in the quantum beat spectrum.

It is important to note that these two interference structures also appear in the range $\Omega < 0$, but the opening of the parabolic

curves is inverted, induced by the fourth term of Eq. (6). Additionally, it should be mentioned that due to the degeneracy of the angular momentum l, contributions from different l states within the same n manifold cannot be distinguished.

3.2. Retrieving the populations of bound states in the hydrogen atom

The horizontal lines correspond to the energy differences of the bound states of the hydrogen atom. In our reconstruction, we specifically focus on the bound states that electrons primarily populate at the end of the first pulse. That is, our goal is to reconstruct the populations of the first four bound states. By referring to the first term of Eq. (6) and the property of the δ-function, we can determine the following values: $\Omega(L_1) \equiv \delta\varepsilon_{21} = \varepsilon_2 - \varepsilon_1 = 0.375$ a.u., $\Omega(L_2) \equiv \delta\varepsilon_{31} = \varepsilon_3 - \varepsilon_1 = 0.444$ a.u., $\Omega(L_3) \equiv \delta\varepsilon_{32} = \varepsilon_3 - \varepsilon_2 = 0.0694$ a.u., and $\Omega(L_4) \equiv \delta\varepsilon_{42} = \varepsilon_4 - \varepsilon_2 = 0.0938$ a.u. Here, L_1, L_2, L_3, L_4 mark the different horizontal lines, as shown in Fig. 3(b). However, due to the finite range of the time delay τ_d in the numerical calculations, the resulting horizontal lines in the quantum beat spectrum have a certain width along Ω. Based on the treatment described in Section 2.2, we can derive a set of equations from Eq. (13),

$$|^1\Lambda_{\mathbf{p}1}||^2\Lambda_{\mathbf{p}1}| = \left| \int_{0.375-d\varepsilon}^{0.375+d\varepsilon} G(\mathbf{p},\Omega)d\Omega \right| \equiv a_1, \qquad (20)$$

$$|^1\Lambda_{\mathbf{p}1}||^3\Lambda_{\mathbf{p}1}| = \left| \int_{0.4444-d\varepsilon}^{0.4444+d\varepsilon} G(\mathbf{p},\Omega)d\Omega \right| \equiv a_2, \qquad (21)$$

$$|^2\Lambda_{\mathbf{p}1}||^3\Lambda_{\mathbf{p}1}| = \left| \int_{0.0694-d\varepsilon}^{0.0694+d\varepsilon} G(\mathbf{p},\Omega)d\Omega \right| \equiv a_3, \qquad (22)$$

$$|^2\Lambda_{\mathbf{p}1}||^4\Lambda_{\mathbf{p}1}| = \left| \int_{0.0938-d\varepsilon}^{0.0938+d\varepsilon} G(\mathbf{p},\Omega)d\Omega \right| \equiv a_4. \qquad (23)$$

The right-hand side of the equations is obtained numerically, where $a_{1(2,3,4)}$ corresponds to the integration of the horizontal lines $L_{1(2,3,4)}$. By solving these four equations, we can obtain the values of $|^1\Lambda_{\mathbf{p}1}|$, $|^2\Lambda_{\mathbf{p}1}|$, $|^3\Lambda_{\mathbf{p}1}|$, and $|^4\Lambda_{\mathbf{p}1}|$. Using time-dependent perturbation theory, we calculate the photoionization cross section [Eq. (14)] for the first four bound states of the hydrogen atom. Combining this with Eq. (11), we can retrieve the populations of the ground state $|1\rangle$, the first excited state $|2\rangle$, the second excited state $|3\rangle$, and the third excited state $|4\rangle$, which are given by $|^1U_{11}|^2$, $|^1U_{21}|^2$, $|^1U_{31}|^2$, and $|^1U_{41}|^2$, respectively.

During the reconstruction process, we obtain different values of p and find that a smaller value of p yields better results ($p = 0.04455$ a.u.). This originates from the fact that the signals are stronger at smaller momenta, which decreases the numerical calculation errors. To further validate the accuracy of our reconstruction method, we introduce changes to the wavelength and optical cycle of the first pulse while keeping the second pulse unchanged ($I_2 = 10^{14}$ W/cm^2, $\omega_2 = 15$ eV, $T_2 = 1$ optical cycle).

In Fig. 4, we compare the reconstructed populations with the results of solving the TDSE. It can be observed that the reconstructed populations closely match the results from the TDSE calculations, demonstrating the effectiveness and accuracy of our reconstruction technique. Compared to the other reconstructed populations, more disagreements always exist for the reconstructed state $|1\rangle$. In addition, the reconstruction error increases as the population of the ground state increases. This can be attributed to the depletion of the ground state, which makes the transition amplitude $^2U_{\mathbf{p}1}$, calculated by the perturbation theory [Eq. (14)], deviate from the actual value slightly.

To investigate the effect of different $d\Omega$ values on the accuracy of the reconstructed populations, we consider a scenario where the first pulse has a wavelength of $\lambda_1 = 100$ nm and a duration of $T_1 = 2.5$ optical cycles. The results are summarized in Table 1. For smaller values of $d\Omega = 0.00102$ a.u., the accuracy of the reconstruction is comparable to that of $d\Omega = 0.00178$ a.u. When we increase $d\Omega$ to 0.00205 a.u., the reconstructed population of state $|4\rangle$ deviates from the result of solving the TDSE. To understand the dependence of the reconstructed populations on $d\Omega$, we analyze the quantum beat at a specific momentum $p = 0.04455$ a.u. in Fig. 5, where $L_{1(2,3,4)}$ corresponds to the horizontal lines shown in Fig. 3. According to Eqs. (20)–(23), the distributions at L_1, L_2, L_3, and L_4 should be separate and isolated peaks to ensure the integration range and accuracy of the reconstructed results. From Fig. 5(c), we can observe that when $d\Omega = 0.00205$ a.u., the distribution at L_3 becomes mixed with other peaks, significantly affecting the accuracy of the reconstructed results. Thus, it is crucial to carefully choose an appropriate value of $d\Omega$ to ensure well-separated peaks in the distributions of the quantum beat spectrum $G(\mathbf{p},\Omega)$ along the horizontal lines, improving the accuracy of the reconstructed populations.
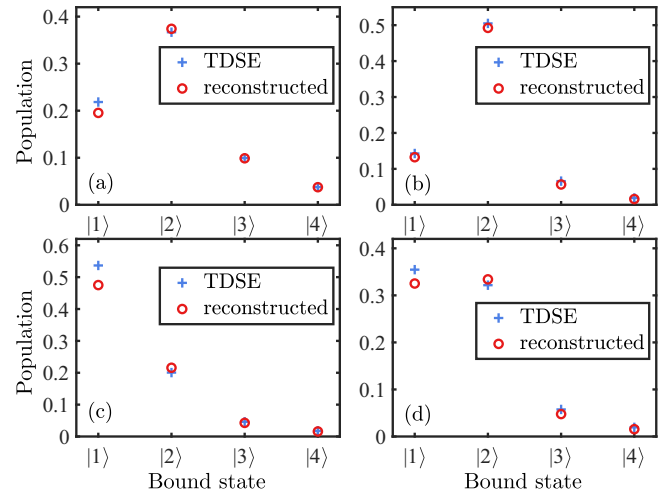

Fig. 4. Populations of the first four bound states calculated by TDSE and reconstructed by our scheme. The laser parameters of the pump pulse are (a) $\lambda_1 = 100$ nm, $T_1 = 2.5$ optical cycles, (b) $\lambda_1 = 120$ nm, $T_1 = 2.5$ optical cycles, (c) $\lambda_1 = 100$ nm, $T_1 = 1.5$ optical cycles, and (d) $\lambda_1 = 120$ nm, $T_1 = 1.5$ optical cycles, respectively. Here, $d\Omega = 0.00178$ a.u.

Table 1. The Constructed Populations for Different Frequency Intervals $d\Omega$ (in a.u.)[a].

	$|1\rangle$	$|2\rangle$	$|3\rangle$	$|4\rangle$
TDSE	0.21843	0.36680	0.099297	0.037572
$d\Omega = 0.00102$	0.20348	0.35930	0.097346	0.039980
$d\Omega = 0.00178$	0.19533	0.37406	0.098829	0.037384
$d\Omega = 0.00205$	0.20011	0.36641	0.097075	0.041837

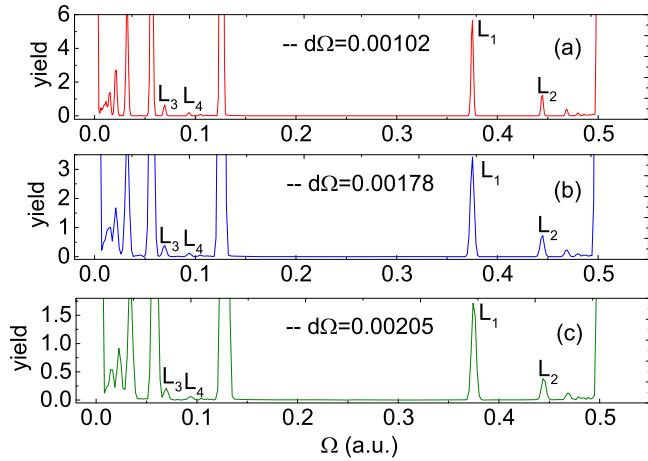[a]The first pulse is $\lambda_1 = 100$ nm and $T_1 = 2.5$ optical cycles.

Fig. 5. The frequency-resolved photoelectron yield at the momentum $p = 0.04455$ a.u. for (a) $d\Omega = 0.00102$ a.u., (b) $d\Omega = 0.0018$ a.u., and (c) $d\Omega = 0.00204$ a.u. L_1, L_2, L_3, L_4 correspond to the horizontal lines in Fig. 3. The first pulse is 100 nm, and the pulse duration is 2.5 optical cycles.

4. Conclusion

In conclusion, we have developed a weak-field-induced quantum beat method that enables the determination of bound state populations, providing in-depth insights into the dynamics of excited states in strong-field phenomena. By applying this method to the strong-field induced ionization of atomic hydrogen, we have effectively validated the accuracy of the reconstructed populations by comparing them with results obtained from the time-dependent Schrödinger equation (TDSE). This approach exhibits the potential for further expansion in investigating complex systems extending beyond hydrogen atom ionization.

Our method focused exclusively on electrons that predominantly occupy the $|1s\rangle$ and $|np\rangle$ states through one-photon transitions induced by the strong pump pulse. To determine the transition amplitude caused by the probe pulse, we included the contributions from these dominant angular momentum states while disregarding those from others. Specifically, we approximated the reconstructed population in the $|2p\rangle$ ($|3p\rangle$,

$|4p\rangle$) state as the population of the $|2\rangle$ ($|3\rangle$, $|4\rangle$) state. Moreover, the photoelectron quantum-beat spectrum is a valuable tool for identifying quantum interference pathways involving bound and continuum states, primarily driven by one-photon transitions. Considering the third term of Eq. (6), extracting information regarding transitions between these continuum states becomes feasible. For future work, we intend to refine our method further to address these limitations, enabling us to accurately interpret the results and understand the information obtained from the beat spectra.

References

1. F. Krausz and M. Ivanov, "Attosecond physics," Rev. Mod. Phys. **81**, 163 (2009).
2. J. A. T. C. Weinacht and P. H. Bucksbaum, "Controlling the shape of a quantum wavefunction," Nature **397**, 233 (1999).
3. P. B. Corkum and F. Krausz, "Attosecond science," Nat. Phys. **3**, 381 (2007).
4. P. Johnsson, J. Mauritsson, T. Remetter, et al., "Attosecond control of ionization by wave-packet interference," Phys. Rev. Lett. **99**, 233001 (2007).
5. M. Lucchini, A. Ludwig, T. Zimmermann, et al., "Anisotropic emission in quantum-beat spectroscopy of helium excited states," Phys. Rev. A **91**, 063406 (2015).
6. R. Pazourek, S. Nagele, and J. Burgdörfer, "Attosecond chronoscopy of photoemission," Rev. Mod. Phys. **87**, 765 (2015).
7. C. D. Lin, A.-T. Le, C. Jin, et al., *Attosecond and Strong-Field Physics: Principles and Applications* (Cambridge University Press, 2018).
8. C.-C. Shu, Y. Guo, K.-J. Yuan, et al., "Attosecond all-optical control and visualization of quantum interference between degenerate magnetic states by circularly polarized pulses," Opt. Lett. **45**, 960 (2020).
9. J. Liang, Y. Zhou, Y. Liao, et al., "Direct visualization of deforming atomic wavefunction in ultraintense high-frequency laser pulses," Ultrafast Sci. **2022**, 9842716 (2022).
10. Z. Lian, S. Luo, H. Qi, et al., "Visualizing ultrafast weak-field-induced rotational revivals of air molecules at room temperature," Opt. Lett. **48**, 411 (2023).
11. M. Hentschel, R. Kienberger, Ch. Spielmann, et al., "Attosecond metrology," Nature **414**, 509 (2001).
12. J. Itatani, F. Quéré, G. L. Yudin, et al., "Attosecond streak camera," Phys. Rev. Lett. **88**, 173903 (2002).
13. V. Véniard, R. Taïeb, and A. Maquet, "Phase dependence of $(N + 1)$-color ($N > 1$) ir-uv photoionization of atoms with higher harmonics," Phys. Rev. A **54**, 721 (1996).
14. K. Klünder, J. M. Dahlström, M. Gisselbrecht, et al., "Probing single-photon ionization on the attosecond time scale," Phys. Rev. Lett. **106**, 143002 (2011).
15. P. M. Paul, E. S. Toma, P. Breger, et al., "Observation of a train of attosecond pulses from high harmonic generation," Science **292**, 1689 (2001).
16. P. Eckle, A. N. Pfeiffer, C. Cirelli, et al., "Attosecond ionization and tunneling delay time measurements in helium," Science **322**, 1525 (2008).
17. A. S. Landsman, M. Weger, J. Maurer, et al., "Ultrafast resolution of tunneling delay time," Optica **1**, 343 (2014).
18. E. Goulielmakis, Z.-H. Loh, A. Wirth, et al., "Real-time observation of valence electron motion," Nature **466**, 739 (2010).

19. R. Santra, V. S. Yakovlev, T. Pfeifer, *et al.*, "Theory of attosecond transient absorption spectroscopy of strong-field-generated ions," Phys. Rev. A **83**, 033405 (2011).
20. R. R. Freeman, P. H. Bucksbaum, H. Milchberg, *et al.*, "Above-threshold ionization with subpicosecond laser pulses," Phys. Rev. Lett. **59**, 1092 (1987).
21. B. Feuerstein, R. Moshammer, D. Fischer, *et al.*, "Separation of recollision mechanisms in nonsequential strong field double ionization of Ar: the role of excitation tunneling," Phys. Rev. Lett. **87**, 043003 (2001).
22. A. Diaspro, P. Bianchini, G. Vicidomini, *et al.*, "Multi-photon excitation microscopy," Biomed. Eng. Online **5**, 36 (2006).
23. T. Streibel and R. Zimmermann, "Resonance-enhanced multiphoton ionization mass spectrometry (REMPI-MS): applications for process analysis," Annu. Rev. Anal. Chem. **7**, 361 (2014).
24. T. Nubbemeyer, K. Gorling, A. Saenz, *et al.*, "Strong-field tunneling without ionization," Phys. Rev. Lett. **101**, 233001 (2008).
25. S. Bengtsson, E. W. Larsen, D. Kroon, *et al.*, "Space–time control of free induction decay in the extreme ultraviolet," Nat. Photonics **11**, 252 (2017).
26. S. Beaulieu, S. Camp, D. Descamps, *et al.*, "Role of excited states in high-order harmonic generation," Phys. Rev. Lett. **117**, 203001 (2016).
27. R. M. Arkhipov, M. V. Arkhipov, I. Babushkin, *et al.*, "Generation of an attosecond pulse based on collective spontaneous radiation emission of a layer of three-level atoms excited by a pair of unipolar pulses," Opt. Spectrosc. **128**, 1857 (2020).
28. R. M. Arkhipov and N. N. Rosanov, "Generation of extremely short pulses of terahertz radiation based on superradiation of a three-level resonant medium," Opt. Spectrosc. **129**, 289 (2021).
29. Y. Chen and B. Zhang, "Role of excited states in the emission times of harmonics from asymmetric molecules," Phys. Rev. A **86**, 023415 (2012).
30. X.-B. Bian and A. D. Bandrauk, "Multichannel molecular high-order harmonic generation from asymmetric diatomic molecules," Phys. Rev. Lett. **105**, 093903 (2010).
31. P. Ranitovic, X. M. Tong, B. Gramkow, *et al.*, "IR-assisted ionization of helium by attosecond extreme ultraviolet radiation," New J. Phys. **12**, 013008 (2010).
32. F. He, C. Ruiz, A. Becker, *et al.*, "Attosecond probing of instantaneous ac stark shifts in helium atoms," J. Phys. B At. Mol. Opt. Phys. **44**, 211001 (2011).
33. C. R. McDonald, G. Orlando, G. Vampa, *et al.*, "Tunnel ionization dynamics of bound systems in laser fields: how long does it take for a bound electron to tunnel?" Phys. Rev. Lett. **111**, 090405 (2013).
34. E. E. Serebryannikov and A. M. Zheltikov, "Strong-field photoionization as excited-state tunneling," Phys. Rev. Lett. **116**, 123901 (2016).
35. M. Klaiber and J. S. Briggs, "Crossover from tunneling to multiphoton ionization of atoms," Phys. Rev. A **94**, 053405 (2016).
36. L. Jia, H. Xing, and L. Fu, "Excited-state resonance tunneling in strong-field ionization," Phys. Rev. A **106**, 022814 (2022).
37. M. P. de Boer and H. G. Muller, "Observation of large populations in excited states after short-pulse multiphoton ionization," Phys. Rev. Lett. **68**, 2747 (1992).
38. M. Sabbar, H. Timmers, Y.-J. Chen, *et al.*, "State-resolved attosecond reversible and irreversible dynamics in strong optical fields," Nat. Phys. **13**, 472 (2017).
39. I. Liontos, S. Cavalieri, C. Corsi, *et al.*, "Ramsey spectroscopy of bound atomic states with extreme-ultraviolet laser harmonics," Opt. Lett. **35**, 832 (2010).
40. D. Z. Kandula, C. Gohle, T. J. Pinkert, *et al.*, "XUV frequency-comb metrology on the ground state of helium," Phys. Rev. A **84**, 062512 (2011).
41. Y. Hikosaka, T. Kaneyasu, M. Fujimoto, *et al.*, "Coherent control in the extreme ultraviolet and attosecond regime by synchrotron radiation," Nat. Commun. **10**, 4988 (2019).
42. W.-C. Jiang, X.-M. Tong, R. Pazourek, *et al.*, "Theory of bound-state coherences generated and probed by optical attosecond pulses," Phys. Rev. A **101**, 053435 (2020).
43. S. X. Hu and L. A. Collins, "Attosecond pump probe: exploring ultrafast electron motion inside an atom," Phys. Rev. Lett. **96**, 073004 (2006).
44. R. Pazourek, M. Reduzzi, P. A. Carpeggiani, *et al.*, "Ionization delays in few-cycle-pulse multiphoton quantum-beat spectroscopy in helium," Phys. Rev. A **93**, 023420 (2016).
45. Y. Zhang, T.-M. Yan, and Y. H. Jiang, "Ultrafast mapping of coherent dynamics and density matrix reconstruction in a terahertz-assisted laser field," Phys. Rev. Lett. **121**, 113201 (2018).
46. L. Xu, H. Dong, and L. Fu, "Frequency-resolved photon-electronic spectroscopy for excited state population detection," Opt. Lett. **43**, 5725 (2018).
47. L. V. Keldysh, "Ionization in the field of a strong electromagnetic wave," Sov. Phys. JETP **20**, 1307 (1965).
48. F. H. M. Faisal, "Multiple absorption of laser photons by atoms," J. Phys. B At. Mol. Opt. Phys. **6**, L89 (1973).
49. H. R. Reiss, "Effect of an intense electromagnetic field on a weakly bound system," Phys. Rev. A **22**, 1786 (1980).
50. D. A. Verner, G. J. Ferland, K. T. Korista, *et al.*, "Atomic data for astrophysics. II. New analytic fits for photoionization cross sections of atoms and ions," Astrophys. J. **465**, 487 (1996).
51. W.-C. Jiang, J.-Y. Shan, Q. Gong, *et al.*, "Virtual sequential picture for nonsequential two-photon double ionization of helium," Phys. Rev. Lett. **115**, 153002 (2015).
52. M. A. Baig, "Measurement of photoionization cross-section for the excited states of atoms: a review," Atoms **10**, 39 (2022).
53. W.-C. Jiang, M.-X. Wang, L.-Y. Peng, *et al.*, "Signatures of stabilization in the angle-resolved photoemission by an ultrashort intense XUV laser pulse," Phys. Rev. A **105**, 023104 (2022).
54. M. Liu, S. U. Khan, X.-Q. Wang, *et al.*, "Roles of the transition amplitude phases in photoelectron asymmetry of single strong attosecond pulse," New J. Phys. **24**, 093019 (2022).
55. W.-C. Jiang and X.-Q. Tian, "Efficient split-Lanczos propagator for strong-field ionization of atoms," Opt. Express **25**, 26832 (2017).
56. S. Wang, W.-C. Jiang, X.-Q. Tian, *et al.*, "Conjoint influence of quantum interference and Freeman resonance on substructures of the photoelectron spectra in above-threshold ionization," Phys. Rev. A **101**, 053417 (2020).
57. W.-C. Jiang, H. Liang, S. Wang, *et al.*, "Enhancing Autler-Townes splittings by ultrafast XUV pulses," Phys. Rev. Res. **3**, L032052 (2021).
58. T. N. Rescigno and C. W. McCurdy, "Numerical grid methods for quantum-mechanical scattering problems," Phys. Rev. A **62**, 032706 (2000).
59. B. I. Schneider and L. A. Collins, "The discrete variable method for the solution of the time-dependent Schrödinger equation," J. Non-Cryst. Solids **351**, 1551 (2005).
60. M. J. Rayson, "Lagrange-Lobatto interpolating polynomials in the discrete variable representation," Phys. Rev. E **76**, 026704 (2007).
61. X. M. Tong, K. Hino, and N. Toshima, "Phase-dependent atomic ionization in few-cycle intense laser fields," Phys. Rev. A **74**, 031405(R) (2006).
62. D. G. Arbó, J. E. Miraglia, M. S. Gravielle, *et al.*, "Coulomb-Volkov approximation for near-threshold ionization by short laser pulses," Phys. Rev. A **77**, 013401 (2008).